Red-absorbing Ru(II) polypyridyl complexes with biotin targeting spontaneously assemble into nanoparticles in biological media

Robin Vinck,[a] Albert Gandioso,[a] Pierre Burckel,[b] Bruno Saubaméa,[c] Kevin Cariou,[a] and Gilles Gasser[a],*

[a]   Chimie ParisTech, PSL University, CNRS, Institute of Chemistry for Life and Health Sciences, Laboratory for Inorganic Chemical Biology, 75005 Paris, France.

[b]   Institut de Physique du Globe de Paris, Biogéochimie à l'Anthropocène des Eléments et Contaminants Emergents, 75005 Paris, France.

[c]   Cellular and Molecular Imaging platform, US 25 Inserm, UMS 3612 CNRS, Faculté de Pharmacie de Paris, Université Paris Cité, 75006 Paris, France.

*   Corresponding author: gilles.gasser@chimieparistech.psl.eu; www.gassergroup.com; Tel. +33 1 85 78 41 51.

ORCID-ID:

Robin Vinck: 0000-0002-2730-0121

Albert Gandioso: 0000-0002-5114-8502

Bruno Saubaméa: 0000-0002-6218-0460

Kevin Cariou: 0000-0002-5854-9632

Gilles Gasser: 0000-0002-4244-5097

ABSTRACT

Four new ruthenium(II) polypyridyl complexes were synthesized to study the effect of poly(ethylene glycol) and/or biotin conjugation on their physical and biological properties, including their hydrophilicity, their cellular uptake, and their phototoxicity. Unexpectedly, these complexes self-assembled into nanoparticles upon dilution in biological media. This behavior leads to their accumulation in lysosomes following their internalization by cells. While a significant increase in cellular uptake was observed for the biotin-conjugated complexes, it did not result in an increase in their phototoxicity. However, their high phototoxicity upon irradiation at long wavelengths (645-670

1

nm) and their self-assembling behavior make them promising backbone for the development of new lysosome-targeted photosensitizers for photodynamic therapy.

INTRODUCTION

The strongest challenge to treat solid tumors is arguably to kill diseased tissues without harming healthy cells. Targeted therapies usually rely on the passive or active targeting of the anticancer agent to the tumor thanks to molecular or supramolecular carriers. These carriers allow for the selective binding of the anticancer agent to the cancer cells, or its accumulation in the tumor vicinity, thus focusing the therapeutic effect and reducing off-target toxicity.[1] Another way to limit the cytotoxic effect to the targeted tissues is to activate an otherwise harmless agent in a site-selective manner. Photodynamic therapy (PDT) relies on this last strategy to limit the cytotoxic effect of a photosensitizer (PS) to the light-irradiated area. Following light-mediated excitation, the photosensitizer transfers the harvested energy to biological components and/or to molecular oxygen to generate highly reactive species, such as singlet oxygen ($^1O_2$) thus inducing localized cellular damages.[2]

In the last few years, our group and others have focused on the development of new metal-based photosensitizers by exploiting the attractive properties of ruthenium polypyridyl complexes, such as their ease of preparation, their stability in biological media and their photophysical properties, including high visible light absorption and $^1O_2$ quantum yields.[2–6] In addition, the physical and biological properties of these complexes can be conveniently fine-tuned by the chemical modification of their ligands.[7] Importantly, increasing the length of the ligand's π- conjugated system have showed to shift the UV-Vis absorption spectrum of related complexes towards higher wavelengths.[8] As higher wavelengths can penetrate deeper into biological tissues, this feature is of particular importance in the treatment of deeply seated tumors.[9] In that respect, our group recently described a long-wavelength absorbing Ru(II) polypyridyl complex with high PDT efficiency in 2D and 3D cancer cell models. The phototoxic effect of [Ru(DIP)$_2$(dmbpy)](Cl)$_2$ (DIP: 4,7-diphenyl-1,10-phenantroline, dmbpy: 4,4'-dimethyl-2,2'-bipyridine) (Figure 1), was achieved following irradiation at 595 nm, which stands close to the ideal wavelength range, also termed "biological window" (600-900 nm). Unfortunately, this promising complex demonstrated a non-negligible toxicity in the dark and no significant selectivity for cancer cells, which could induce adverse effects in (pre)clinical settings.[10] Additionally, preliminary attempts at dissolving it in carriers compatible with intravenous injections at pharmaceutically relevant concentrations failed due to an aggregation behavior. We therefore thought that further engineering of this prototypical complex would be necessary to afford a PDT PS with real therapeutical potential.

In order to prevent off-target toxicity, we reasoned that this complex could benefit from an active targeting to cancer cells. Many strategies have been employed to target Ru(II) polypyridyl complexes to tumors.[11] Amongst these strategies, we chose the conjugation of the complex with biotin (vitamin B$_8$), which would yield a relatively simple complex with a selective uptake in cancer cells. Indeed, the Sodium-dependent MultiVitamin Transporter (SMVT), largely responsible for the uptake of biotin, is overexpressed in many cancerous cell lines *in vitro*. This could be explained by the fact that quickly dividing cancer cells require a higher nutrient uptake. Conjugating antitumor agents to biotin has thus been extensively explored, often leading to enhanced uptake and cytotoxicity in cancer cells.[12] This strategy has also been applied to metal-based PSs. In some examples, the PS was encapsulated in biotin-conjugated nanocarriers.[13–15] Although these strategies yielded a higher cellular uptake and phototoxicity in cancer cells in comparison to healthy cells, the complexity of these multi-component systems might hamper the development of a potential drug candidate. On the other hand, direct conjugation of a biotin moiety on a Ru(II) PS has also been recently explored by Chao and co-workers and Chakravarty and co-workers.[16,17] However, in order to achieve phototoxicity in the biological window, two-photon irradiation and the addition of a BODIPY moiety was required respectively.

In line with these previous successes, and considering the promising features of [Ru(DIP)$_2$(dmbpy)](Cl)$_2$, we thought this latter strategy would yield a structurally simple and efficient photosensitizer. In

addition, as polyvalent ligand-receptor interactions can yield binding affinities orders of magnitude higher in comparison to a monovalent interaction, we thought that incorporating two biotin moieties in the complex would further improve its binding to SMVTs, and thus its cellular internalization.[18] Finally, we hypothesized that integrating a poly(ethylene glycol) (PEG) chain into the structure of the complex could help with improving its aqueous solubility. A series of Ru(II) polypyridyl complexes based on the structure of the prototypical complex [Ru(DIP)$_2$(dmbpy)](Cl)$_2$ and incorporating either no PEG chain nor biotin residue (**1**), two PEG chains but no biotin residue (**2**), no PEG chain but two biotin residues (**3**) and two PEG chains and two biotin residues (**4**) were synthesized and their (photo)physical and biological properties were investigated.
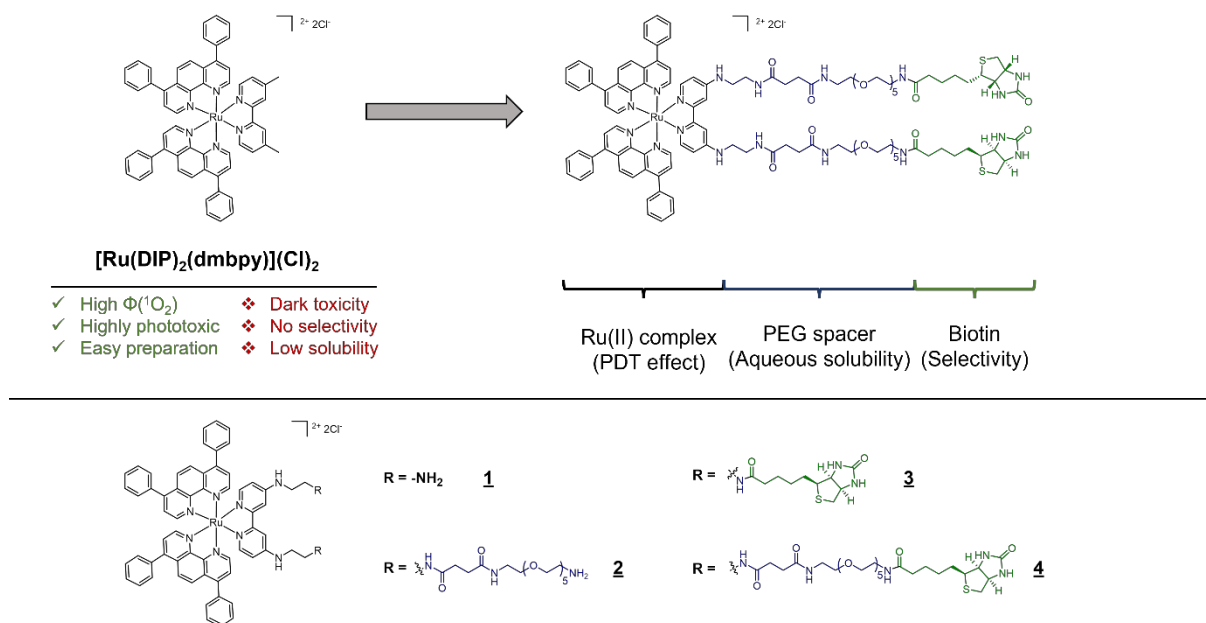

Figure 1. Structures of the prototypical complex [Ru(DIP)$_2$(dmbpy)](Cl)$_2$, molecular design of a biotin functionalized targeted PS and structure of complexes **1**-**4**.

RESULTS AND DISCUSSION

The precursor complexes Ru(DIP)$_2$(Cl)$_2$, [Ru(DIP)$_2$(4,4'-dibromo-2,2'-bypiridine)](PF$_6$)$_2$ and the BOC-protected linker 2,2-dimethyl-4,24-dioxo-3,8,11,14,17,20-hexaoxa-5,23-diazaheptacosan-27-oic acid were synthesized according to reported procedures.[19–22] The size of the PEG chain was chosen as a good compromise between solubilizing properties and commercial availability of the monodispersed hexaethylene glycol precursor. Complex **1** was obtained *via* aromatic nucleophilic substitution by heating the precursor complex [Ru(DIP)$_2$(4,4'-dibromo-2,2'-bypiridine)](PF$_6$)$_2$ at 150 °C in neat ethylene diamine. A simple precipitation from the ethylene diamine using a saturated solution of ammonium hexafluorophosphate (NH$_4$PF$_6$) in water followed by a chromatographic purification allowed to isolate complex **1** with an 89% yield. Complex **1** was coupled with the protected linker using classical amide bond formation techniques using hexafluorophosphate azabenzotriazole tetramethyl uronium (HATU) as a coupling agent followed by a trifluoroacetic acid-mediated deprotection to afford complex **2** with a quantitative yield. These coupling conditions were chosen to allow the isolation of the pure complexes from the crude mixture by a simple precipitation using NH$_4$PF$_6$. Complex **3** was obtained in a similar way with a 74% yield by coupling **1** with biotin. Finally, coupling of complex **2** with biotin afforded complex **4** with a 77% yield (Scheme S1). All complexes were primarily isolated as PF$_6^-$ salts but were converted to chloride salts to improve their aqueous solubility. The structure of the final

complexes was confirmed by ^{1}H and ^{13}C NMR and HRMS and their purity was assessed by elemental analysis and HPLC (see supporting information). Of note, final complexes were obtained as hydrochloride salts as evidenced by the elemental analyses.

To assess the effect of both PEG and biotin moieties on the hydrophilicity of complexes **1-4**, their partition coefficient between water and octanol (LogP) was determined (Figure 2.A). As expected, complex **2** demonstrated an improved partition in water in comparison to **1** thanks to its PEG moieties. On the other hand, **3** appeared to be significantly more lipophilic than **1**, which is probably due to the inherent lipophilic nature of biotin. Overall, both PEG and biotin moieties appeared to compensate for each other's effect on the hydrophilicity of complex **4**. While all four complexes displayed a preferential distribution in water over octanol, as shown by their negative LogP, only complexes **1**, **2**, and **4** appeared fully soluble in water at all tested concentrations (> 10 mM). In contrast, **3** was only soluble at lower concentrations (< 2 mM). However, when complexes were diluted in phosphate buffer saline pH 7.4 (PBS), **1**, **3**, and **4** formed large visible aggregates even at low concentrations (100 µM). This behavior might be due to the reduction of the electrostatic repulsion between positively charged complexes induced by a solvent with a high ionic strength such as PBS (Figure 2.C). This phenomenon has already been observed in the case of gold nanoparticles. While negatively charged gold nanoparticle colloids were stabilized by electrostatic repulsions, their aggregation could be triggered in the presence of salts.[23] In the case of complexes **1-4**, this aggregation behavior resulted in an inversion of the sign of the LogP, with a preferential partition in the octanol phase. With a LogP(PBS) close to 0, complex **2** suffered the least from this phenomenon, which could be attributed to the solubilizing nature of the PEG chains.
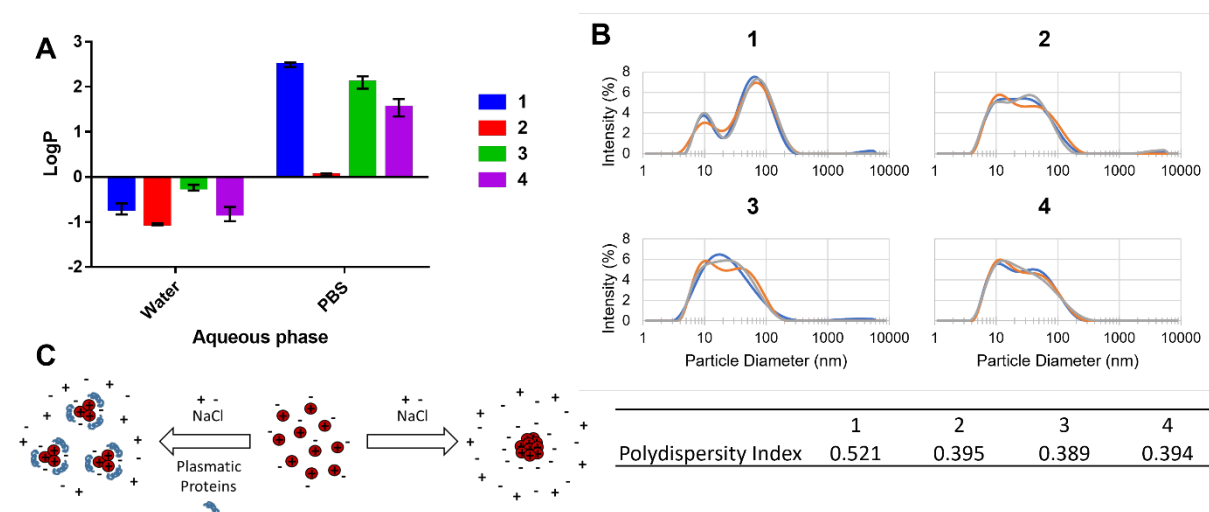

Figure 2. Solubility and aggregation behavior of complexes **1-4**. **A**. Partition coefficient of complexes **1-4** (50 µM) between octanol and aqueous phases. Results are presented as mean ± SD of three independent replicates. Of note, no significant difference was found in the molar extinction coefficient of the complexes at 450 nm in octanol and water. **B**. DLS data: particle size distribution by intensity of complexes **1-4** (20 µM) in 10% FBS in PBS. The three curves represent three measurements of the same sample. The table indicates the polydispersity indexes of the corresponding nanoparticles. **C**. Schematic representation of the aggregation behavior of complexes **1-4**. When subjected to increasing concentration of salts, Van der Waals attractive forces overcome repulsive electrostatic interactions, leading to the formation of large aggregates. Through a coating effect, plasmatic proteins stabilize small particles and further prevent their aggregation.

However, as described in the case of gold nanoparticles, the formation of large aggregates was prevented by the addition of plasmatic proteins in the solvent.[23] Similarly, when diluted in 10% Fetal

Bovine Serum (FBS) in PBS, no visible aggregates could be observed for all four complexes. However, a dynamic light scattering (DLS) analysis further revealed the presence of particles with a large polydispersity (4-350 nm) for all complexes (Figure 2.B). While plasmatic proteins could not completely prevent the formation of aggregates, their coating effect might contribute to the stabilization of the complexes as nanoparticles, thus preventing their precipitation (Figure 2.C).

The cellular uptake of complexes **1-4** was then evaluated on the A549 (human lung carcinoma), CT26 (mouse colon carcinoma), HEK-293 (human embryonic kidney cells) and RPE-1 (immortalized human retinal pigment epithelium) cell lines by inductively coupled plasma mass spectrometry (ICP-MS). As shown in Fig. 3.A, complexes **1**, **2**, and **4** were taken up in a comparable manner. In contrast, complex **3**, appeared to accumulate *ca*. 10 times more than the other complexes. As a higher lipophilicity can usually be associated with a better cellular uptake, these results could be solely explained by the lipophilic nature of complex **3**. However, as shown in Fig 3.B, preincubating cells with a 20-fold excess of free D-biotin prior to treatment with the complexes led to a 2.7 and 8.8-fold decrease in the cellular uptake of complexes **3**, and **4**, respectively, while it had no significant effect on the uptake of complexes **1** and **2**. Interestingly, following this pretreatment, the uptake of **3** appeared in the same range to that of **1**. These results suggest that complexes **3** and **4** are partly internalized following a SMVT-dependent route. The lower contribution of biotin to the internalization of **4** in comparison of **3** might be explained by the steric hindrance induced by the PEG spacers. Multivalent interactions of **3** with surface expressed SMVTs could also lead to a higher binding affinity, which could in turn explain its higher cellular uptake. Of note, no cell line-specific internalization behavior was observed, as each complex appeared to be taken up by all four cell lines in a similar manner. While this was expected for complexes **1** and **2**, the SMVT-dependent internalization of **3** and **4** was expected to impart them with some degree of selectivity for cancer cells (A549 and CT26 cell lines) over non-cancerous cell lines (HEK-293 and RPE-1). The ability of the tested cell lines to take up biotin was therefore further evaluated by confocal microscopy using a fluorescent biotin probe. As shown in Figure 3.C, A549 and CT26 cells did not appear to take up the probe significantly more than RPE-1 and HEK-293 cells, although a small but significant difference could be observed between CT26 and A549 cells.
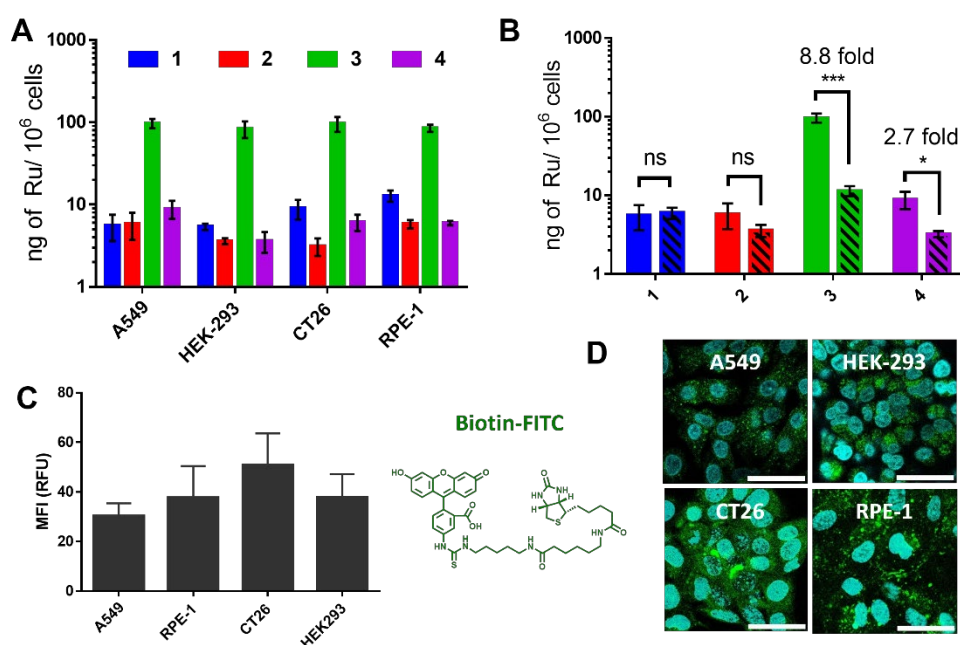

Figure 3. Cellular uptake of complexes **1-4**. **A**. Cellular uptake of complexes **1-4** (5 μM, 4 h) in A549 (human lung carcinoma), CT26 (mouse colon carcinoma), RPE-1 (human retinal pigmented epithelial), and HEK-293 (human embryonic kidney) cells determined by ICP-MS. Results are presented as mean ±

SD of three independent experiments. **B**. Cellular uptake of complexes **1**-**4** (5 µM, 4 h) in A549 cells following preincubation with medium (plain bars) or 100 µM of D-biotin (dashed bars). Results are presented as mean ± SD of three independent replicates. ns: non-significant, ***: $p < 0.001$, *: $p < 0.05$, non-parametric t-test. **C**. Cellular uptake of a fluorescent biotin probe (Biotin-FITC) in A549, RPE-1, CT26, and HEK-293 cells measured by fluorescence confocal microscopy. Results are presented as a mean ± SD of the green fluorescence signal (exc: 488 nm, em: 508-539 nm) of at least 50 individual cells. **D**. Representative confocal microscopy images of cells incubated with biotin-FITC (green) and Hoechst 33342 (cyan). The scale bars represent 40 µm.

To further investigate the internalization mechanism of complexes **1**-**4**, their subcellular localization was determined by confocal microscopy using the intrinsic luminescence of our Ru(II) complexes. Preliminary tests suggested that the complexes accumulate in well-defined intracellular compartments. A549 cells were therefore co-incubated with complexes **1**-**4** and a lysosome-targeted tracker (Lysotracker™ Deep Red). After 4 hours of incubation, all four complexes appeared to accumulate in lysosomes, as the complexes colocalized well with the tracker (Figure 4). The complexes also appeared to accumulate in other compartments, which can be inferred as endosomes, from which lysosomes originate. These data suggest that complexes **1**-**4** are taken up by endocytosis and end up in the lysosomes. As a member of the solute carrier family, SMVTs are known to mediate the direct transport of biotin from the extracellular space directly to the cytoplasm.[24] However, none of the biotin-conjugated complexes appeared to localize there. This could be explained by the bulky nature of these complexes, which prevents their trafficking through the transporter. On the other hand, nanoparticles are known to be taken up by pinocytosis, which would explain the common subcellular distribution of the four complexes.[25,26] Additionally, complex **3** was also found at the cell membrane, although the corresponding signal appeared faint (Figure S19). Taken altogether, these results suggest that complexes **1**-**4** share a common uptake mechanism, excluding a SMVT-dependent internalization of complexes **3** and **4**. The strong binding of the biotin-conjugated complexes to the extracellular domain of SMVTs might, however, increase their local concentration at the cell membrane, thus promoting their uptake by endocytosis.

Taken together with the results the cellular uptake study, this overall suggests that biotin-functionalized Ru(II) complexes have the potential to selectively target cancer cells overexpressing SMVTs, but not through a SMVT-dependent internalization. Yet, the cell lines selected in this study may not be ideal models to confirm this hypothesis. Knockout cell lines and/or cell lines modified to constitutively overexpress SMVTs may be alternatively used as models, although one could argue that these engineered cells strongly deviate from the pathological reality.
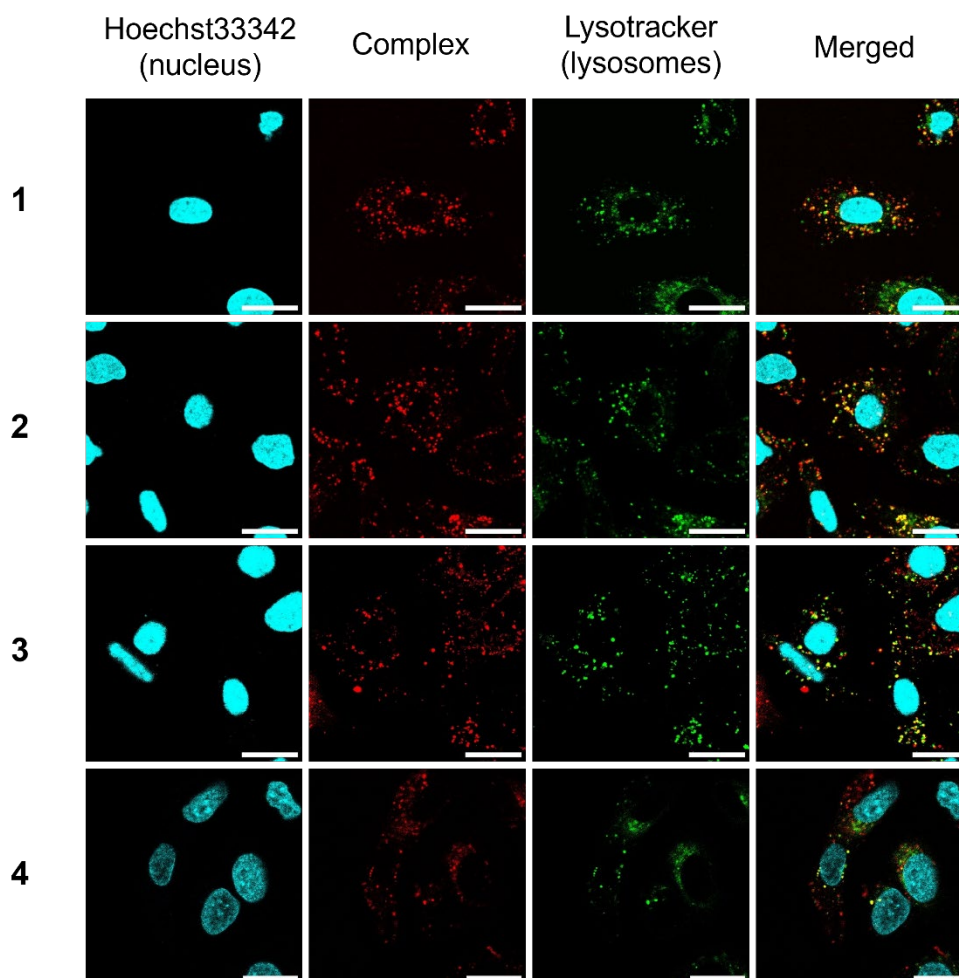
Figure 4. Confocal microscopy images of A549 cells incubated with complexes **1-4** (red, exc: 448 nm, em: 645-730 nm), the nucleus dye Hoechst 33342 (cyan, exc: 405 nm, em: 409-448 nm), and the lysosome-specific dye Lysotracker® Deep Red (green, exc: 638 nm, em: 693-708 nm). Colocalization is indicated in yellow. The scale bars represent 20 μm.

These findings are of particular importance as it has been shown that the subcellular localization of a PS is critical to its phototoxicity. While the nucleus and the mitochondria are frequently targeted for their crucial role in the cell life cycle, lysosomes have also been considered as candidates for organelle-targeted PDT.[27] Indeed, the PDT-mediated destabilization of lysosomes can lead to cell death through apoptosis and/or necrosis.[28–32]

In addition to its cellular uptake and subcellular localization, the photophysical properties of a PS, including its $^1O_2$ quantum yield (ϕ^1O_2) and light absorption (ideally in the biological window) are critical to its PDT potential. Upon irradiation at 450 nm, the ϕ^1O_2 of the four complexes was determined in CH_3CN by measuring the characteristic light signal emitted when the produced $^1O_2$ relaxes into triplet oxygen. Complexes **1-4** exhibited a satisfying ϕ^1O_2 in the range 0.49-0.66, which is similar to the reported ϕ^1O_2 of 0.61 for [Ru(DIP)$_2$(dmbpy)](Cl)$_2$ (Figure 5.A).[10] The UV-Vis spectra of **1-4** recorded in ethanol were almost identical and revealed a bathochromic shift of the metal to ligand charge transfer band in regards to [Ru(DIP)$_2$(dmbpy)](Cl)$_2$ with a small, yet non-negligible absorbance at up to ≈ 650 nm (Figure 5.B).[10]
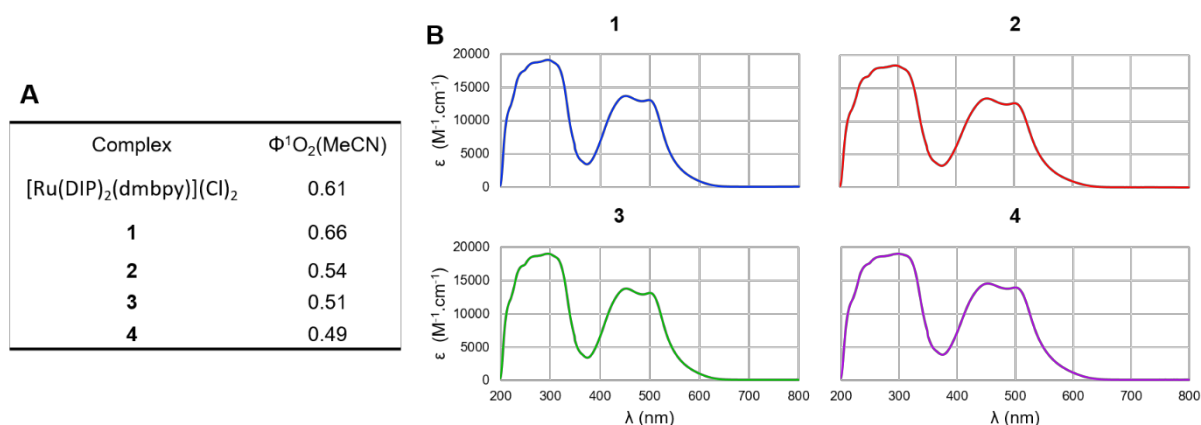
Figure 5. Photophysical properties of complexes **1**-**4**. A. Singlet oxygen quantum yields measured in CH$_3$CN. B. UV-Vis absorption spectra measured in ethanol.

The phototoxicity of these PSs was thus evaluated following 4 hours of incubation and 1 hour of irradiation at 645 nm on A549, HEK-293, CT26 and RPE-1 cells. The toxicity of the complexes in the dark was also measured following 4 hours of incubation with the complexes. Using these data, the phototoxicity index (PI), defined as the ratio between the concentration necessary to kill 50% of the cells (IC$_{50}$) in the dark and the IC$_{50}$ following light irradiation was calculated. Interestingly, complexes **2**-**4** appeared significantly less toxic in the dark in comparison to **1**, although this difference was less clear on HEK-293 cells (Figure 6.A). Following light irradiation at 645 nm, however, complexes **1**-**4** displayed a comparable and intense phototoxicity with IC$_{50}$s ranging from 0.2 to 1.4 µM, resulting in superior average PIs for complexes **2**-**4** (Figure 6.B-C). Surprisingly, despite its superior cellular uptake, complex **3** did not demonstrate a significantly superior toxicity (both in the dark and upon light irradiation). This could be explained by a sequestration of the complex to the cell membrane, as evidenced by the confocal microscopy study, which would limit the access to its intracellular target. Another explanation could involve the stability of the nanoparticles formed by the complexes. While **1** and **2** display two primary amines which would help the disintegration of the aggregates in the acidic lysosomes, and while the PEG chains confer a superior hydrophilicity to **4**, the aggregates formed by the hydrophobic complex **3** might not fully dissolve in the lysosomes, which could reduce its ability to photosensitize oxygen. Importantly, complexes **1** and **3** appeared to be phototoxic even upon irradiation at 670 nm for 1 hour (12.6 J/cm^2), with IC$_{50}$ of 2.2 ± 0.9 and 2.0 ± 0.9 µM, respectively.
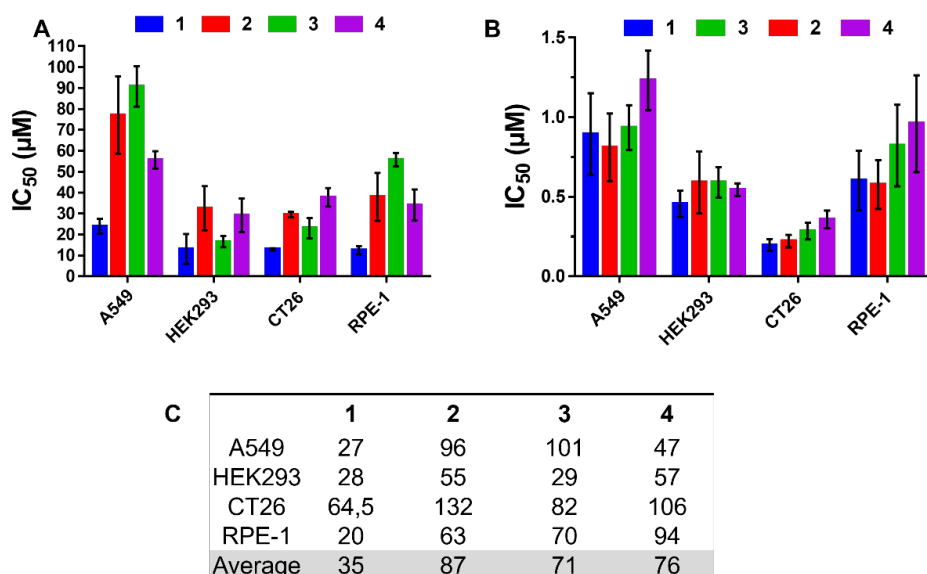
Figure 6. *In vitro* PDT efficiency of complexes **1-4** in A549, HEK293, CT26, and RPE-1 cells. A. Toxicity in the dark. B. Toxicity following irradiation at 645 nm for 1 h (7.6 J/cm²). Results are presented as a mean ± SD of three independent replicates. C. Phototoxicity indexes for complexes **1-4**.

C	1	2	3	4
A549	27	96	101	47
HEK293	28	55	29	57
CT26	64,5	132	82	106
RPE-1	20	63	70	94
Average	35	87	71	76

CONCLUSIONS

Previous research works demonstrated the efficiency of conjugating targeting moieties to PSs in enhancing their cellular uptake or specific subcellular localization. In the present study, biotin-targeting initially appeared to enhance the SMVT-dependent cellular uptake of our Ru(II) polypyridyl complexes. Additional experiments however demonstrated that biotin might promote the binding of the complexes at the cell membrane, without directly inducing their SMVT-dependent uptake. While some uncertainty remains regarding the absence of correlation between the cellular uptake and the phototoxicity of the complexes, it appears clear that, in this case, biotin may not be the targeting moiety of choice especially owing to its deleterious effect on the hydrophilicity of the compounds. We were however surprised by the spontaneous aggregation behavior of the complexes in aqueous media containing plasmatic proteins. Our group and others previously described the aggregation behavior of structurally related Ru(II) or iridium complexes when diluted from a solvent to a non-solvent.[33–38] In contrast, the phenomenon described in the present study occurs upon increasing the salt concentration in the aqueous phase. This was previously observed in the case of amphiphilic ruthenium complexes bearing a chloride ion as a ligand.[39] In this case however, this phenomenon was attributed to the stabilization of the chloride ligand, preventing the hydration of the complex in the aqueous phase, thus reducing its solubility and inducing its aggregation. Of note, in these studies, the aggregation of Ru(II) polypyridyl complexes were accompanied by an increase in their phosphorescence. This effect, called the aggregation-induced emission, is of interest when developing imaging agents. However, this effect may not be desired when developing PDT PSs, as radiative decay of the triplet state of the PS competes with its quenching by molecular oxygen to produce $^1O_2$. Nevertheless, in the case of complexes **1-4** these unexpected "self-assembled" nanoparticles appeared to selectively accumulate in lysosomes. This phenomenon could be exploited to design other lysosome-directed PDT systems while varying the nature of the targeting unit to optimize the cancer cell selectivity. Alternatively, these systems could be conjugated to peptides promoting their endosomal escape, or even their nuclear localization. Such complexes would be internalized as

nanoparticles by endocytosis and would then be directed to other subcellular compartments to optimize their phototoxicity. Finally, the complexes developed herein demonstrated a significant phototoxicity upon irradiation at 670 nm, which is relatively rare for Ru(II) polypyridyl complexes.[40] In conclusion, although biotin-targeting did not appear to give satisfying results in this study, it allowed to uncover a new backbone with great promise in the search of new metal-based PDT PSs.

EXPERIMENTAL SECTION

Materials

All chemicals were obtained from commercial sources and were used without further purification. Ru(DIP)$_2$Cl$_2$, [Ru(DIP)$_2$(4,4'-dibromo-2,2-bipyridine)] [PF$_6$]$_2$, and the protected linker 2,2-dimethyl-4,24-dioxo-3,8,11,14,17,20-hexaoxa-5,23-diazaheptacosan-27-oic acid was prepared as previously described.[19–22] Spectroscopic data were in accordance with the literature.

Instrumentation and methods

^{1}H- and ^{13}C-NMR spectra were recorded on a 400 MHz NMR spectrometer (Bruker). Chemical shifts (δ) are reported in parts per million (ppm) referenced to tetramethylsilane (δ 0.00) ppm using the residual proton solvent peaks as internal standards. Coupling constants (*J*) are reported in Hertz (Hz) and the multiplicity is abbreviated, as follows: s (singlet), d (doublet), and m (multiplet). Electrospray Ionization-Mass Spectrometry (ESI-HRMS) experiments were carried out using a LTQ-Orbitrap XL from Thermo Scientific (Thermo Fisher Scientific) and operated in positive ionization mode, with a spray voltage at 3.6 kV. No sheath and auxiliary gas was used. Applied voltages were 40 and 100 V for the ion transfer capillary and the tube lens, respectively. The ion transfer capillary was held at 275 °C. Detection was achieved in the Orbitrap with a resolution set to 100,000 (at *m/z* 400) and an *m/z* range between 150 and 2000 in profile mode. Spectrum was analyzed using the acquisition software XCalibur 2.1 (Thermo Fisher Scientific). The automatic gain control (AGC) allowed for the accumulation of up to $2 \cdot 10^5$ ions for Fourier Transform Mass Spectrometry (FTMS) scans, maximum injection time was set to 300 ms and 1 µs scan was acquired. 10 µL was injected using a Thermo Finnigan Surveyor HPLC system (Thermo Fisher Scientific) with a continuous infusion of methanol at 100 µL·min^{-1}. Elemental microanalyses were performed on a Thermo Flash 2000 elemental analyzer. UV-Vis absorbance spectrum were recorded in quartz cuvette using a Cary 4000 UV-Vis spectrometer (Agilent). HPLC analysis was performed using two Agilent G1361 1260 Prep Pump, an Agilent G7115A 1260 DAD WR detector equipped with an Agilent Pursuit XRs 5C18 (100 Å, C18 5 µm 250 × 4.6 mm) column. The flow rate was 1 mL/min with the following gradient: 0–3 min: isocratic 95% A (5 % B); 3–17 min: linear gradient from 95% A (5% B) to 0 %A (100% B); 17–23 min: isocratic 0% A (100% B). The solvents (HPLC grade) were Millipore water (0.1 % TFA, solvent A) and acetonitrile (solvent B). Chromatogram were detected at 215, 250, 350, 450, and 550 nm. The solvents (HPLC grade) were Millipore water (solvent A) and acetonitrile (solvent B). 0–3 min: isocratic 95% A (5 % B); 3–17 min: linear gradient from 95% A (5% B) to 0 %A (100% B); 17–23 min: isocratic 0% A (100% B).

Synthesis

[Ru(4,7-diphenyl-1,10-phenanthroline)$_2$(N1,N1'-([2,2'-bipyridine]-4,4'-diyl)bis(ethane-1,2-diamine))][PF$_6$]$_2$ (1)

[Ru(DIP)$_2$(4,4'-dibromo-2,2'-bipyridine)][PF$_6$]$_2$ (250 mg, 0.18 mmol, 1.0 equiv.) was suspended in ethylenediamine (2 mL). The mixture was heated at 180 °C in a sealed tube for 15 min. A saturated solution of NH$_4$PF$_6$ was added (2 mL) and the solid was filtered and washed extensively with water and diethyl ether. The product was isolated by column chromatography on silica gel with a CH$_3$CN/aqueous KNO$_3$ (0.4 M) solution (10:1). The fractions containing the product were collected and the solvent was removed. The residue was dissolved in CH$_3$CN and undissolved KNO$_3$ was removed by filtration. The solvent was removed, and the product was dissolved in H$_2$O. A saturated solution of NH$_4$PF$_6$ was added and the solid was filtered and washed extensively with water and diethyl ether to yield **1** as a red

powder (260 mg, 0.16 mmol, 89%). ^{1}H-NMR (CD$_3$CN, 400 MHz): δ = 8.50 (d, J = 5.5 Hz, 2H), 8.18 (q, J = 9.5 Hz, 4H), 8.10 (d, J = 5.5 Hz, 2H), 7.82 (d, J = 5.5 Hz, 2H), 7.75-7.54 (m, 22H), 7.53 (d, J = 5.5 Hz, 2H), 7.15 (d, J = 6.5 Hz, 2H), 6.48 (dd, J = 6.61, 2.55 Hz, 2H), 5.96 (t, J = 5.6 Hz, 2H), 3.30 (q, J = 5.9 Hz, 4H), 2.88 (t, J = 6.0 Hz, 4H). ^{13}C-NMR (CD$_3$CN, 100 MHz): δ = 157.9, 155.9, 153.1, 152.8, 151.0, 149.9, 149.0, 137.0, 136.8, 130.9, 130.8, 130.54, 130.49, 130.12, 130.06, 130.0, 127.04, 126.95, 126.9, 126.8, 45.7, 41.2. ESI-HRMS (pos. detection mode): calcd for C$_{62}$H$_{52}$N$_{10}$Ru m/z [M]$^{2+}$ 519.1704; found: 519.1704. 50 mg of this PF$_6$ salt was converted into a Cl salt using amberlite IRA-410 to yield 30 mg of a red powder. Elemental analysis calcd for C$_{62}$H$_{54}$N$_{10}$Cl$_2$Ru·4HCl·4H$_2$O (%): C 56.12, H 4.86, N 10.56; found: C 56.52, H 4.89, N 10.33.

[Ru(4,7-diphenyl-1,10-phenanthroline)$_2$(N1,N1'-(([2,2'-bipyridine]-4,4'-diylbis(azanediyl))bis(ethane-2,1-diyl))bis(N4-(17-amino-3,6,9,12,15-pentaoxaheptadecyl)succinamide))$_2$][PF$_6$]$_2$ (2)

Under nitrogen, 2,2-dimethyl-4,24-dioxo-3,8,11,14,17,20-hexaoxa-5,23-diazaheptacosan-27-oic acid (100 mg, 0.208 mmol, 2.8 equiv.) and hexafluorophosphate azabenzotriazole tetramethyl uronium (HATU, 100 mg, 0.263 mmol, 3.5 equiv.) were dissolved in anhydrous DMF (2 mL). The mixture was mixed for 30 min at room temperature. A solution of DIPEA (0.080 mL, 0.456 mmol, 6.1 equiv.) and **1** (120 mg, 0.075 mmol, 1.0 equiv.) in DMF (1 mL) was added and the mixture was agitated for 15 h at room temperature in the dark. A saturated aqueous solution of NH$_4$PF$_6$ was added and the mixture was kept at 4 °C for 2 h. The solid was filtered and washed with water and diethyl ether. The solid was dissolved in dichloromethane (5 mL) and TFA was added (1 mL). The mixture was agitated for 5 h at r.t. in the dark. The solvent was evaporated to dryness and the residue was dissolved in methanol (5 mL). A saturated aqueous solution of NH$_4$PF$_6$ was added and the mixture was kept at 4 °C for 16 h. The solid was filtered and washed with water and diethyl ether to give **2** as a red powder (140 mg, 0.075, quant). 40 mg of this PF$_6$ salt was converted to the chloride salt using Amberlite IRA 410. ^{1}H-NMR (Methanol-d_4, 400 MHz): δ = 8.50 (d, J = 5.5 Hz, 2H), 8.18 (q, J = 9.5 Hz, 4H), 8.10 (d, J = 5.6 Hz, 2H), 7.85 (d, J = 5.5 Hz, 2H), 7.68 – 7.60 (m, 4H), 7.61 – 7.42 (m, 22H), 7.06 (d, J = 6.4 Hz, 2H), 6.50 (dd, J = 6.4, 2.0 Hz, 2H), 3.65 – 3.24 (m, 56H), 3.02 (dd, J = 5.7, 4.5 Hz, 4H), 2.38 (dd, J = 8.9, 3.9 Hz, 8H). ^{13}C-NMR (Methanol-d_4, 100 MHz): δ = 176.6, 175.3, 174.6, 153.4, 153.2, 153.1, 150.30, 150.26, 149.8, 137.3, 137.2, 131.1, 131.0, 130.8, 130.7, 130.3, 130.23, 130.15, 127.5, 127.4, 127.32, 127.26, 71.5, 71.3, 71.0, 70.6, 67.9, 42.72, 42.68, 40.6, 40.3, 39.30, 32.27, 32.1. ESI-HRMS (pos. detection mode): calcd for C$_{94}$H$_{112}$N$_{14}$O$_{14}$Ru m/z [M]$^{2+}$ 881.3757; found: 881.3781. Elemental analysis calcd for C$_{94}$H$_{112}$N$_{14}$O$_{14}$RuCl$_2$·4HCl·6H$_2$O (%): C 53.63, H 6.18, N 9.39; found: C 53.34, H 5.80, N 9.68.

[Ru(4,7-diphenyl-1,10-phenanthroline)$_2$(5-((3aR,4R,6aS)-2-oxohexahydro-1H-thieno[3,4-d]imidazol-4-yl)-N-(2-((4'-((2-(5-((3aS,4S,6aR)-2-oxohexahydro-1H-thieno[3,4-d]imidazol-4-yl)pentanamido)ethyl)amino)-[2,2'-bipyridin]-4-yl)amino)ethyl)pentanamide)$_2$][PF$_6$]$_2$ (3)

Under nitrogen, D-biotin (30 mg, 0.123 mmol, 4.0 equiv.) and HATU (70 mg, 0.185 mmol, 6.0 equiv.) were dissolved in anhydrous DMF (2 mL). The mixture was mixed for 30 min at room temperature. A solution of DIPEA (0.042 mL, 0.247 mmol, 8.0 equiv.) and **1** (50 mg, 0.031 mmol, 1 equiv.) in DMF (1 mL) was added and the mixture was agitated for 15 h at room temperature in the dark. A saturated aqueous solution of NH$_4$PF$_6$ was added and the mixture was kept at 4 °C for 2 h. The solid was filtered and washed with water and diethyl ether. The solid was dissolved in a small amount of MeCN, and filtered. The solvent was evaporated and the solid dried under vacuum to give **3** as a red powder (41 mg, 0.023 mmol, 74%). The PF$_6$ salt was converted to the chloride salt using Amberlite IRA 410. ^{1}H-NMR (Methanol-d_4, 400 MHz): δ = 8.60-8.57 (m, 2H), 8.29 (q, J = 9.4 Hz, 4H), 8.20 (d, J = 5.4 Hz, 2H), 7.97 (dd, J = 5.5, 1.9 Hz, 4H), 7.89 – 7.47 (m, 26H), 7.19-7.16 (m, 2H), 6.60 (d, J = 4.8 Hz, 2H), 4.47 – 4.43 (m, 2H), 4.27 – 4.23 (m, 2H), 3.55-3.35 (m, 8H), 3.20-3.00 (m, 2H), 2.83 (td, J = 12.5, 4.9 Hz, 2H),

2.61 (dd, J = 20.3, 12.7 Hz, 2H), 2.27 – 2.12 (m, 4H), 1.71 – 1.19 (m, 14H). ^{13}C-NMR (Methanol-d_4, 100 MHz): δ = 176.6, 166.0, 156.6, 153.2, 153.0, 150.3, 149.8, 137.3, 137.2, 131.1, 131.0, 130.8, 130.3, 130.2, 127.5, 127.43, 127.36, 127.2, 63.3, 61.6, 57.0, 42.7, 41.0, 39.7, 39.63, 39.59, 39.53, 39.47, 29.8, 29.5, 26.8. ESI-HRMS (pos. detection mode): calcd for $C_{82}H_{80}N_{14}O_4S_2Ru$ m/z $[M]^{2+}$ 745.2480; found: 745.2494. Elemental analysis calcd for $C_{82}H_{80}Cl_2N_{14}O_4RuS_2$·2HCl·6H$_2$O (%): C 56.51, H 5.44, N 11.25, S 3.68; found: C 56.24, H 5.42, N 11.37, S 3.33.

[Ru(4,7-diphenyl-1,10-phenanthroline)$_2$(N1-(19-oxo-23-((3aR,4R,6aS)-2-oxohexahydro-1H-thieno[3,4-d]imidazol-4-yl)-3,6,9,12,15-pentaoxa-18-azatricosyl)-N4-(2-((4'-((4,7,27-trioxo-31-((3aS,4S,6aR)-2-oxohexahydro-1H-thieno[3,4-d]imidazol-4-yl)-11,14,17,20,23-pentaoxa-3,8,26-triazahentriacontyl)amino)-[2,2'-bipyridin]-4-yl)amino)ethyl)succinamide)$_2$][PF$_6$]$_2$ (4)

Under nitrogen, D-biotin (46 mg, 0.188 mmol, 4.0 equiv.) and HATU (107 mg, 0.282 mmol, 6.0 equiv.) were dissolved in anhydrous DMF (2 mL). The mixture was mixed for 30 min at room temperature. A solution of DIPEA (0.064 mL, 0.376 mmol, 8.0 equiv.) and **2** (100 mg, 0.047 mmol, 1 equiv.) in DMF (1 mL) was added and the mixture was agitated for 15 h at room temperature in the dark. A saturated aqueous solution of NH$_4$PF$_6$ was added and the mixture was kept at 4 °C for 2 h. The solid was filtered and washed with water and diethyl ether. The solid was dissolved in a small amount of MeCN, and filtered. The solvent was evaporated and the solid dried under vacuum to give **4** as a red powder (90 mg, 0.036, 77%). The PF$_6$ salt was converted to the chloride salt using Amberlite IRA 410. ^{1}H-NMR (Methanol-d_4, 400 MHz): δ = 8.61 (d, J = 5.5 Hz, 2H), 8.30 (q, J = 9.5 Hz, 4H), 8.21 (d, J = 5.6 Hz, 2H), 7.97 (d, J = 5.5 Hz, 4H), 7.79 – 7.54 (m, 26H), 7.18 (d, J = 6.8 Hz, 2H), 6.60 (d, J = 6.2 Hz, 2H), 4.48 (dd, J = 7.9, 4.9 Hz, 2H), 4.29 (dd, J = 7.9, 4.5 Hz, 2H), 3.69 – 3.38 (m, 52H), 3.30 (d, J = 5.5 Hz, 4H), 3.21 – 3.15 (m, 2H), 2.90 (ddd, J = 12.7, 4.9, 1.9 Hz, 2H), 2.68 (d, J = 12.7 Hz, 2H), 2.56 – 2.41 (m, 8H), 2.27 – 2.12 (m, 4H), 1.82 – 1.49 (m, 8H), 1.47 – 1.32 (m, 6H).^{13}C-NMR (Acetonitrile-d_3, 100 MHz): δ = 174.3, 173.9, 173.2, 164.3, 156.0, 153.1, 152.8, 152.7, 150.6, 150.52, 150.47, 149.83, 149.80, 148.93, 148.89, 136.7, 136.8, 130.9, 130.8, 130.5, 130.1, 130.0, 129.7, 127.1, 127.0, 126.9, 126.8, 71.0, 70.8, 70.2, 62.4, 60.9, 56.3, 42.9, 41.1, 40.0, 39.8, 38.9, 36.2, 32.1, 31.9, 28.9, 26.3. ESI-HRMS (pos. detection mode): calcd for $C_{114}H_{140}N_{18}O_{18}S_2Ru$ m/z $[M]^{2+}$ 1107.4533; found: 1107.4537. Elemental analysis calcd for $C_{114}H_{140}N_{18}O_{18}S_2RuCl_2$·2HCl·4H$_2$O (%): C 56.31, H 6.22, N 10.37, S 2.64; found: C 56.16, H 6.04, N 10.53, S 2.33.

Singlet oxygen

The samples were prepared in an air saturated CH$_3$CN solution with an absorbance of 0.2 at 450 nm. This solution was irradiated in fluorescence quartz cuvettes (width 1 cm) using a mounted M450LP1 LED (Thorlabs) whose irradiation, centered at 450 nm, has been focused with aspheric condenser lenses. The intensity of the irradiation has been varied using a T-Cube LED Driver (Thorlabs) and measured with an optical power and energy meter. The emission signal was focused and collected at right angle to the excitation pathway and directed to a Princeton Instruments Acton SP-2300i monochromator. A longpass glass filter was placed in front of the monochromator entrance slit to cut off light at wavelengths shorter than 850 nm. As a detector an EO-817L IR-sensitive liquid nitrogen cooled germanium diode detector (North Coast Scientific Corp.) has been used. The singlet oxygen luminesce at 1270 nm was measured by recording spectra from 1100 to 1400 nm. For the data analysis, the singlet oxygen luminescence peaks at different irradiation intensities were integrated. The resulting areas were plotted against the percentage of the irradiation intensity and the slope of the linear regression calculated. The absorbance of the sample was corrected with an absorbance correction factor. As reference for the measurement phenalenone (Φ = 96%) was used and the singlet oxygen quantum yields were calculated using the following formula:

$$\Phi_{sample} = \Phi_{reference} * (S_{sample} / S_{reference}) * (I_{reference} / I_{sample})$$

$$I = I_0 * (1 - 10^{-A})$$

Φ = singlet oxygen quantum yield, S = slope of the linear regression of the plot of the areas of the singlet oxygen luminescence peaks against the irradiation intensity, I = absorbance correction factor, I_0 = light intensity of the irradiation source, A = absorbance of the sample at irradiation wavelength.

Partition coefficient

The aqueous phase (MilliQ water or DPBS) was saturated for 24 hours with octanol. The octanol phase was saturated for 24 hours with the aqueous phase. 1 mL of a 50 µM solution of the complex in the aqueous phase was added to 1 mL of the octanol phase. The mixture was agitated for 24 hours in the dark. The layers were then separated, and the corrected absorbance at 450 nm in each phase was measured. The logP was calculated as follows:

$$LogP = \log \left(\frac{Absorbance_{450}(Octanol)}{Absorbance_{450}(Aqueous\ phase)} \right)$$

DLS analysis

The nanoparticles size distributions by intensity and the polydispersity indexes were determined by dynamic light scattering (DLS) using a Malvern ZetaSizer Nano ZS (scattering angle = 173°) at a temperature of 25°C with an equilibrium time of 120 s. 2mM stock solutions of the complexes in MilliQ water were filtered on a 0.22 µm membrane and were diluted at a concentration of 20 µM in filtered 10% FBS in PBS.

Inductively Coupled Plasma Mass Spectrometry

Elemental concentrations were assessed using an Agilent 7900 quadrupole ICP-MS. Ru isotopes of mass 99 and 101 were measured without collision gas for better sensitivity. Both isotopes provide the same Ru elemental concentrations confirming the absence of isobaric interferences. An indium internal-standard was injected after inline mixing with the samples to correct for signal drift and matrix effects. A set of 5 Ru calibration standards was analyzed to confirm and model (through simple linear regression) the linear relationship between signal and concentration. The model was then used to convert measured sample counts to concentrations. Reported uncertainties were calculated using error propagation equations and considering the combination of standard deviation on replicated consecutive signal acquisitions (n = 3), internal-standard ratio and blank subtraction. The non-linear term (internal-standard ratio) was linearized using a first-order Taylor series expansion to simplify error propagation.

Cell culture

A549, HEK-293 and CT26 cells were cultured in DMEM medium (Gibco, Life Technologies, USA) supplemented with 10 % of fetal calf serum (Gibco). RPE-1 cells were cultured in DMEM/F-12 medium

(Gibco) supplemented with 10 % of fetal calf serum. All cell lines were complemented with 100 U/mL penicillin-streptomycin mixture (Gibco) and maintained in humidified atmosphere at 37 °C and 5 % of CO_2. All experiments were performed in DMEM as its formulation does not include D-biotin.

Cellular uptake

4.10^6 cells were seeded in 10-cm petri dishes (10 mL/dish) and were incubated at 37 °C, 5% CO_2. The next day, the medium was replaced with 5 µM of complexes dilution in 10 mL of culture medium and the dishes were incubated for 4 hours at 37 °C, 5% CO_2. Cells were washed three times with cold PBS, trypsinized, harvested, and a 10 µL aliquot of each cell suspension was sampled for accurate counting. The cell suspensions were centrifuged, and the supernatant was discarded. The pellets were digested in 100 µL of 70% HNO_3 at 65 °C for 24 h and then diluted in 5 mL of MilliQ water (final HNO_3 concentration: 1.4 %). The Ru content in each sample was determined by ICP-MS. For pre-incubation experiments, cells were incubated with 100 µM of D-biotin in 10 mL of culture medium for 1 hour. The medium was then replaced by a solution containing 100 µM of D-biotin and 5 µM of the complexes in 10 mL of culture medium. The experiment was then performed as described above.

Biotin-probe uptake

Cells were seeded in confocal dishes (VWR®) and incubated overnight at 37 °C, 5% CO_2. The next day the culture medium was replaced with a 10 µM solution of biotin-FITC (Santa Cruz Biotechnology, sc-214340). The cells were incubated for 2 hours. 10 min before the end of the incubation period, one drop of a Hoechst 33342 solution (NucBlue™ Live ReadyProbes™ Reagent, Invitrogen™) was added to the dishes. Cells were then washed three times with cold PBS and imaged within 5 minutes on a SP5 confocal microscope (Leica, Wetzlar, Germany). The Hoechst 33342 was excited at 405 nm and the signal was integrated in the range 409-448 nm. The Biotin-FITC was excited at 488 nm and the fluorescence signal was integrated in the range 508-539 nm. Several images of each dish were acquired. Images were treated using the ImageJ software. The mean FITC fluorescence signal of at least 50 cells/cell line was measured and the background signal was subtracted.

Subcellular localization by confocal microscopy

Cells were seeded in confocal dishes (VWR®) and incubated overnight at 37 °C, 5% CO_2. The next day the culture medium was replaced with 5 µM dilutions of the complexes in culture medium and the dishes were incubated in the dark for 4 hours. 1 hour before the end of the incubation time, the Lysotracker® Deep Red (Invitrogen®) was added at a final concentration of 75 nM. 10 minutes before the end of the incubation time, one drop of a Hoechst 33342 solution (NucBlue™ Live ReadyProbes™ Reagent, Invitrogen™) was added to the dishes. Cells were then washed three times with cold PBS and imaged within 5 minutes on a SP5 confocal microscope (Leica, Wetzlar, Germany). The Hoechst 33342 was excited at 405 nm and the signal was integrated in the range 409-448 nm. The complexes were excited at 448 nm and the fluorescence signal was integrated in the range em: 645-730 nm. The Lysotracker® Deep Red was excited at 638 nm and the fluorescence signal was integrated in the range em: 693-708 nm. Images were treated using the ImageJ software.

(Photo-)cytotoxicity

Cells were seeded at a 4,000 cells/well density in 96-well plates (100 µL/well) and were incubated at 37 °C, 5% CO_2 for 24 h. The medium was then replaced with test compound dilutions in fresh medium (100 µL/well) and cells were incubated at 37 °C, 5% CO_2 for 4 h. The medium was replaced by 100 µL of fresh medium. Plates were then irradiated at 645 or 670 nm for 1 hour at 37 °C (7.6 and 12.6 J/cm²)

using a LUMOS-BIO photoreactor (Atlas Photonics). For dark toxicity experiments, plates were instead kept in the dark for 1 hour at 37°C, 0% CO_2. Cells were then incubated for an additional 44 h at 37 °C, 5% CO_2. The medium was replaced with 100 μL of fresh medium containing resazurin (0.2 mg/mL). After 4h of incubation at 37 °C, 5% CO_2, plates were read using a SpectraMaxM2 Microplate Reader (λ_{exc} = 540 nm; λ_{read} = 590 nm). Fluorescence data were normalized, data were fitted using GraphPad Prism Software and IC_{50} was calculated by non-linear regression.

Conflicts of interest

The authors declare no competing financial interests.

SUPPORTING INFORMATION

Scheme of synthesis (S1). ^{1}H and ^{13}C NMR spectra (Fig. S1-S8). ESI-HRMS spectra (Fig. S9-S12). HPLC chromatograms (Fig. S13-S16. Enlarged confocal microscopy images of the subcellular localization of complexes in A549 cells.

REFERENCES

(1)   Vyas, D.; Patel, M.; Wairkar, S. Strategies for Active Tumor Targeting-an Update. *Eur. J. Pharmacol.* **2022**, *915*, 174512. https://doi.org/10.1016/j.ejphar.2021.174512.

(2)   Monro, S.; Colón, K. L.; Yin, H.; Roque, J.; Konda, P.; Gujar, S.; Thummel, R. P.; Lilge, L.; Cameron, C. G.; McFarland, S. A. Transition Metal Complexes and Photodynamic Therapy from a Tumor-Centered Approach: Challenges, Opportunities, and Highlights from the Development of TLD1433. *Chem. Rev.* **2019**, *119* (2), 797–828. https://doi.org/10.1021/acs.chemrev.8b00211.

(3)   McFarland, S. A.; Mandel, A.; Dumoulin-White, R.; Gasser, G. Metal-Based Photosensitizers for Photodynamic Therapy: The Future of Multimodal Oncology? *Curr. Opin. Chem. Biol.* **2020**, *56*, 23–27. https://doi.org/10.1016/j.cbpa.2019.10.004.

(4)   Heinemann, F.; Karges, J.; Gasser, G. Critical Overview of the Use of Ru(II) Polypyridyl Complexes as Photosensitizers in One-Photon and Two-Photon Photodynamic Therapy. *Acc. Chem. Res.* **2017**, *50* (11), 2727–2736. https://doi.org/10.1021/acs.accounts.7b00180.

(5)   Knoll, J. D.; Turro, C. Control and Utilization of Ruthenium and Rhodium Metal Complex Excited States for Photoactivated Cancer Therapy. *Coord. Chem. Rev.* **2015**, *282–283*, 110–126. https://doi.org/10.1016/j.ccr.2014.05.018.

(6)   Mari, C.; Pierroz, V.; Ferrari, S.; Gasser, G. Combination of Ru(II) Complexes and Light: New Frontiers in Cancer Therapy. *Chem. Sci.* **2015**, *6* (5), 2660–2686. https://doi.org/10.1039/C4SC03759F.

(7)   Vinck, R.; Karges, J.; Tharaud, M.; Cariou, K.; Gasser, G. Physical, Spectroscopic, and Biological Properties of Ruthenium and Osmium Photosensitizers Bearing Diversely Substituted 4,4′-Di(Styryl)-2,2′-Bipyridine Ligands. *Dalton Trans.* **2021**, *50* (41), 14629–14639. https://doi.org/10.1039/D1DT02083H.

(8)   Karges, J.; Kuang, S.; Maschietto, F.; Blacque, O.; Ciofini, I.; Chao, H.; Gasser, G. Rationally Designed Ruthenium Complexes for 1- and 2-Photon Photodynamic Therapy. *Nat. Commun.* **2020**, *11* (1), 3262. https://doi.org/10.1038/s41467-020-16993-0.

(9)   Barun, V. V.; Ivanov, A. P.; Volotovskaya, A. V.; Ulashchik, V. S. Absorption Spectra and Light Penetration Depth of Normal and Pathologically Altered Human Skin. *J. Appl. Spectrosc.* **2007**, *74* (3), 430–439. https://doi.org/10.1007/s10812-007-0071-2.

(10)   Karges, J.; Heinemann, F.; Jakubaszek, M.; Maschietto, F.; Subecz, C.; Dotou, M.; Vinck, R.; Blacque, O.; Tharaud, M.; Goud, B.; Viñuelas-Zahinos, E.; Spingler, B.; Ciofini, I.; Gasser, G. Rationally Designed Long-Wavelength Absorbing Ru(II) Polypyridyl Complexes as Photosensitizers for Photodynamic Therapy. *J. Am. Chem. Soc.* **2020**, *142* (14), 6578–6587. https://doi.org/10.1021/jacs.9b13620.

(11)   Martínez-Alonso, M.; Gasser, G. Ruthenium Polypyridyl Complex-Containing Bioconjugates. *Coord. Chem. Rev.* **2021**, *434*, 213736. https://doi.org/10.1016/j.ccr.2020.213736.

(12)   Maiti, S.; Paira, P. Biotin Conjugated Organic Molecules and Proteins for Cancer Therapy: A Review. *Eur. J. Med. Chem.* **2018**, *145*, 206–223. https://doi.org/10.1016/j.ejmech.2018.01.001.

(13)   Huang, Y.; Huang, W.; Chan, L.; Zhou, B.; Chen, T. A Multifunctional DNA Origami as Carrier of Metal Complexes to Achieve Enhanced Tumoral Delivery and Nullified Systemic Toxicity. *Biomaterials* **2016**, *103*, 183–196. https://doi.org/10.1016/j.biomaterials.2016.06.053.

(14) Chan, L.; Huang, Y.; Chen, T. Cancer-Targeted Tri-Block Copolymer Nanoparticles as Payloads of Metal Complexes to Achieve Enhanced Cancer Theranosis. *J Mater Chem B* **2016**, *4* (26), 4517–4525. https://doi.org/10.1039/C6TB00514D.

(15) Karges, J.; Li, J.; Zeng, L.; Chao, H.; Gasser, G. Polymeric Encapsulation of a Ruthenium Polypyridine Complex for Tumor Targeted One- and Two-Photon Photodynamic Therapy. *ACS Appl. Mater. Interfaces* **2020**, *12* (49), 54433–54444. https://doi.org/10.1021/acsami.0c16119.

(16) Li, J.; Zeng, L.; Xiong, K.; Rees, T. W.; Jin, C.; Wu, W.; Chen, Y.; Ji, L.; Chao, H. A Biotinylated Ruthenium(II) Photosensitizer for Tumor-Targeted Two-Photon Photodynamic Therapy. *Chem. Commun.* **2019**, *55* (73), 10972–10975. https://doi.org/10.1039/C9CC05826E.

(17) Paul, S.; Kundu, P.; Bhattacharyya, U.; Garai, A.; Maji, R. C.; Kondaiah, P.; Chakravarty, A. R. Ruthenium(II) Conjugates of Boron-Dipyrromethene and Biotin for Targeted Photodynamic Therapy in Red Light. *Inorg. Chem.* **2020**, *59* (1), 913–924. https://doi.org/10.1021/acs.inorgchem.9b03178.

(18) Varner, C. T.; Rosen, T.; Martin, J. T.; Kane, R. S. Recent Advances in Engineering Polyvalent Biological Interactions. *Biomacromolecules* **2015**, *16* (1), 43–55. https://doi.org/10.1021/bm5014469.

(19) Sullivan, B. P.; Salmon, D. J.; Meyer, T. J. Mixed Phosphine 2,2'-Bipyridine Complexes of Ruthenium. *Inorg. Chem.* **1978**, *17* (12), 3334–3341. https://doi.org/10.1021/ic50190a006.

(20) Nakagawa, A.; Ito, A.; Sakuda, E.; Fujii, S.; Kitamura, N. Emission Tuning of Heteroleptic Arylborane–Ruthenium(II) Complexes by Ancillary Ligands: Observation of Strickler–Berg-Type Relation. *Inorg. Chem.* **2018**, *57* (15), 9055–9066. https://doi.org/10.1021/acs.inorgchem.8b01058.

(21) Shinchi, H.; Komaki, F.; Yuki, M.; Ohara, H.; Hayakawa, N.; Wakao, M.; Cottam, H. B.; Hayashi, T.; Carson, D. A.; Moroishi, T.; Suda, Y. Glyco-Nanoadjuvants: Impact of Linker Length for Conjugating a Synthetic Small-Molecule TLR7 Ligand to Glyco-Nanoparticles on Immunostimulatory Effects. *ACS Chem. Biol.* **2022**, *17* (4), 957–968. https://doi.org/10.1021/acschembio.2c00108.

(22) Singh, S.; Oyagawa, C. R. M.; Macdonald, C.; Grimsey, N. L.; Glass, M.; Vernall, A. J. Chromenopyrazole-Based High Affinity, Selective Fluorescent Ligands for Cannabinoid Type 2 Receptor. *ACS Med. Chem. Lett.* **2019**, *10* (2), 209–214. https://doi.org/10.1021/acsmedchemlett.8b00597.

(23) Albanese, A.; Chan, W. C. W. Effect of Gold Nanoparticle Aggregation on Cell Uptake and Toxicity. *ACS Nano* **2011**, *5* (7), 5478–5489. https://doi.org/10.1021/nn2007496.

(24) The International Transporter Consortium; Giacomini, K. M.; Huang, S.-M.; Tweedie, D. J.; Benet, L. Z.; Brouwer, K. L. R.; Chu, X.; Dahlin, A.; Evers, R.; Fischer, V.; Hillgren, K. M.; Hoffmaster, K. A.; Ishikawa, T.; Keppler, D.; Kim, R. B.; Lee, C. A.; Niemi, M.; Polli, J. W.; Sugiyama, Y.; Swaan, P. W.; Ware, J. A.; Wright, S. H.; Wah Yee, S.; Zamek-Gliszczynski, M. J.; Zhang, L. Membrane Transporters in Drug Development. *Nat. Rev. Drug Discov.* **2010**, *9* (3), 215–236. https://doi.org/10.1038/nrd3028.

(25) Ren, W. X.; Han, J.; Uhm, S.; Jang, Y. J.; Kang, C.; Kim, J.-H.; Kim, J. S. Recent Development of Biotin Conjugation in Biological Imaging, Sensing, and Target Delivery. *Chem. Commun.* **2015**, *51* (52), 10403–10418. https://doi.org/10.1039/C5CC03075G.

(26) Mosquera, J.; García, I.; Liz-Marzán, L. M. Cellular Uptake of Nanoparticles versus Small Molecules: A Matter of Size. *Acc. Chem. Res.* **2018**, *51* (9), 2305–2313. https://doi.org/10.1021/acs.accounts.8b00292.

(27) Wang, R.; Li, X.; Yoon, J. Organelle-Targeted Photosensitizers for Precision Photodynamic Therapy. *ACS Appl. Mater. Interfaces* **2021**, *13* (17), 19543–19571. https://doi.org/10.1021/acsami.1c02019.

(28) Zhou, Z.; Liu, J.; Huang, J.; Rees, T. W.; Wang, Y.; Wang, H.; Li, X.; Chao, H.; Stang, P. J. A Self-Assembled Ru–Pt Metallacage as a Lysosome-Targeting Photosensitizer for 2-Photon Photodynamic Therapy. *Proc. Natl. Acad. Sci.* **2019**, *116* (41), 20296–20302. https://doi.org/10.1073/pnas.1912549116.

(29) Daugelaviciene, N.; Grigaitis, P.; Gasiule, L.; Dabkeviciene, D.; Neniskyte, U.; Sasnauskiene, A. Lysosome-Targeted Photodynamic Treatment Induces Primary Keratinocyte Differentiation. *J. Photochem. Photobiol. B* **2021**, *218*, 112183. https://doi.org/10.1016/j.jphotobiol.2021.112183.

(30) Zhou, Y.; Zhang, D.; He, G.; Liu, C.; Tu, Y.; Li, X.; Zhang, Q.; Wu, X.; Liu, R. A Lysosomal Targeted NIR Photosensitizer for Photodynamic Therapy and Two-Photon Fluorescence Imaging. *J. Mater. Chem. B* **2021**, *9* (4), 1009–1017. https://doi.org/10.1039/D0TB02692A.

(31) Sudheesh, K. V.; Jayaram, P. S.; Samanta, A.; Bejoymohandas, K. S.; Jayasree, R. S.; Ajayaghosh, A. A Cyclometalated IrIII Complex as a Lysosome-Targeted Photodynamic Therapeutic Agent for Integrated Imaging and Therapy in Cancer Cells. *Chem. – Eur. J.* **2018**, *24* (43), 10999–11007. https://doi.org/10.1002/chem.201801918.

(32) Niu, N.; Zhou, H.; Liu, N.; Jiang, H.; Hussain, E.; Hu, Z.; Yu, C. A Smart Perylene Derived Photosensitizer for Lysosome-Targeted and Self-Assessed Photodynamic Therapy. *Chem. Commun.* **2019**, *55* (8), 1036–1039. https://doi.org/10.1039/C8CC09396B.

(33) Notaro, A.; Gasser, G.; Castonguay, A. Note of Caution for the Aqueous Behaviour of Metal-Based Drug Candidates. *ChemMedChem* **2020**, *15* (4), 345–348. https://doi.org/10.1002/cmdc.201900677.

(34) Babu, E.; Mareeswaran, P. M.; Krishnan, M. M.; Sathish, V.; Thanasekaran, P.; Rajagopal, S. Unravelling the Aggregation Induced Emission Enhancement in Tris(4,7-Diphenyl-1,10-Phenanthroline)Ruthenium(II) Complex. *Inorg. Chem. Commun.* **2018**, *98*, 7–10. https://doi.org/10.1016/j.inoche.2018.09.035.

(35) Sheet, S. K.; Sen, B.; Patra, S. K.; Rabha, M.; Aguan, K.; Khatua, S. Aggregation-Induced Emission-Active Ruthenium(II) Complex of 4,7-Dichloro Phenanthroline for Selective Luminescent Detection and Ribosomal RNA Imaging. *ACS Appl. Mater. Interfaces* **2018**, *10* (17), 14356–14366. https://doi.org/10.1021/acsami.7b19290.

(36) Elemans, J. A. A. W.; Rowan, A. E.; Nolte, R. J. M. Hierarchical Self-Assembly of Amphiphilic Metallohosts to Give Discrete Nanostructures. *J. Am. Chem. Soc.* **2002**, *124* (7), 1532–1540. https://doi.org/10.1021/ja012061i.

(37) Chen, Y.; Qiao, L.; Yu, B.; Li, G.; Liu, C.; Ji, L.; Chao, H. Mitochondria-Specific Phosphorescent Imaging and Tracking in Living Cells with an AIPE-Active Iridium(III) Complex. *Chem. Commun.* **2013**, *49* (94), 11095–11097. https://doi.org/10.1039/C3CC46957C.

(38) Siewert, B.; van Rixel, V. H. S.; van Rooden, E. J.; Hopkins, S. L.; Moester, M. J. B.; Ariese, F.; Siegler, M. A.; Bonnet, S. Chemical Swarming: Depending on Concentration, an Amphiphilic Ruthenium Polypyridyl Complex Induces Cell Death via Two Different Mechanisms. *Chem. – Eur. J.* **2016**, *22* (31), 10960–10968. https://doi.org/10.1002/chem.201600927.

(39) Siewert, B.; Langerman, M.; Hontani, Y.; Kennis, J. T. M.; Rixel, V. H. S. van; Limburg, B.; Siegler, M. A.; Saez, V. T.; Kieltyka, R. E.; Bonnet, S. Turning on the Red Phosphorescence of a [Ru(Tpy)(Bpy)(Cl)]Cl Complex by Amide Substitution: Self-Aggregation, Toxicity, and

Cellular Localization of an Emissive Ruthenium-Based Amphiphile. *Chem. Commun.* **2017**, *53* (81), 11126–11129. https://doi.org/10.1039/C7CC02989F.

(40) Lifshits, L. M.; Iii, J. A. R.; Konda, P.; Monro, S.; Cole, H. D.; Dohlen, D. von; Kim, S.; Deep, G.; Thummel, R. P.; Cameron, C. G.; Gujar, S.; McFarland, S. A. Near-Infrared Absorbing Ru(II) Complexes Act as Immunoprotective Photodynamic Therapy (PDT) Agents against Aggressive Melanoma. *Chem. Sci.* **2020**, *11* (43), 11740–11762. https://doi.org/10.1039/D0SC03875J.

In biological media, a series of new red-absorbing Ru(II) polypyridyl complexes self-assemble into nanoparticles which are taken up by endocytosis by cancer cells, leading to their accumulation in lysosomes. Following irradiation at 670 nm, the complexes exhibited a high phototoxicity in the low micromolar range. Biotin-targeting increased the complexes cellular uptake, but counterintuitively did not improve their selectivity towards cancer cells.